Liu, Z.-R.R., Zhou, M.-F., Williams-Jones, A.E., Wang, W., Gao, J.-F., 2019.
Diagenetic mobilization of Ti and formation of brookite/anatase in early Cambrian black shales, South China.
Chemical Geology, 506: 79-96.

Diagenetic mobilization of Ti and formation of brookite/anatase in early Cambrian black shales, South China

Ze-Rui Ray Liu[1], Mei-Fu Zhou[1*], Anthony E. Williams-Jones[2], Wei Wang[3], Jian-Feng Gao[4]

1 Department of Earth Sciences, the University of Hong Kong, Pokfulam Road, Hong Kong, China

2 Department of Earth and Planetary Sciences, McGill University, 3450 University Street, Montreal, QC H3A 0E8, Canada

3 State Key Laboratory of Geological Processes and Mineral Resources, School of Earth Sciences, China University of Geosciences, Wuhan 430074, China

4 State Key Laboratory of Ore Deposit Geochemistry, Institute of Geochemistry, Chinese Academy of Sciences, Guiyang 550081, China

*Corresponding author: Mei-Fu Zhou

E-mail: mfzhou@hku.hk

Phone: +852 2857 8251

Abstract

Titanium (Ti) is typically hosted in detrital minerals in marine sediments and has long been considered to be immobile during diagenesis. In this study, the authigenic titania minerals, brookite and anatase, are observed in early Cambrian carbonaceous shales from the Meishucun and Zhajin sections of South China, respectively. Black shales in the Meishucun section have total organic carbon (TOC) contents from 1.6 to 3.9 wt% and HI (hydrogen index) values from 3.8 to 20, whereas black shales in the Zhajin section have much higher TOC (7.1 − 15.6 wt%) but lower HI (<2.0) and contain abundant bitumen (~3 vol%). Brookite in black shales from the Meishucun section crystallized invariably along cleavages of detrital biotite. This intimate association suggests that the Ti required to form titania minerals was derived from detrital biotite and that Ti was mobilized only on a nano- to micro-meter scale. In contrast, anatase aggregates in black shales from the Zhajin section are intergrown with bitumen. It is proposed that Ti in these shales was mobilized in low pH organic-rich fluids and with increasing pH later precipitated preferentially as anatase. The mobilization of Ti in black shales is indicative of chemical variation of carbonaceous rocks during diagenetic or post-diagenetic processes. Our study demonstrates that proxies using geochemical data for black shales can employed to estimate redox conditions in ancient oceans, but must be applied with caution.

Keywords: Brookite, Anatase, Ti mobility, Ti-mineralization, Black shales, South China

1 Introduction

Authigenic titania minerals are rare in marine sediments due to the low concentration (0.005 to 0.35nM) of Ti in seawater (Skrabal, 2006; Van Den Berg et al., 1994) and the inert behavior of detrital Ti- minerals (Cornu et al., 1999). Titanium is thus considered to be immobile in marine sediments, and is thought to be a useful proxy for estimating the proportion of detrital components and sedimentary provenance (e.g., Young and Nesbitt, 1998; Wen et al., 2011). The notion of Ti immobility, however, has been challenged by recent observations that authigenic titania minerals are present in organic-rich sediments (e.g., Fuchs et al., 2015; Schulz et al., 2016). Indeed, it has been proposed that large amounts of Ti can be dissolved in organic carbon-rich waters/fluids (Parnell, 2004; Cabral et al., 2012), but the sources of Ti and specific mechanisms of Ti-migration and precipitation remain unknown.

Authigenic titania minerals in organic-rich shales/siltstones consist dominantly of fine-grained brookite and anatase (Schulz et al., 2016), which display different growth habits from those formed by artificial synthesis. During syntheses of nano-crystalline TiO_2 solids, anatase is the first phase to crystallize due to its low surface energy, but it is typically replaced by a more stable phase, brookite, when the grain-size exceeds 11 nm (Zhang and Banfield, 2014). On heating to temperature > 600°C, both anatase and brookite are converted to rutile (Byrne et al., 2013), the only stable form of TiO_2 solids at all physico-chemical conditions encountered in the Earth's crust (Zhang and Banfield, 2014). In organic-rich shales/siltstones, however, TiO_2 is commonly present

as anatase, which generally crystallizes within bitumen (Fuchs et al., 2015), or is found at oil-water contacts (Schulz et al., 2016); whereas the occurrence of brookite is restricted in sediments of lower thermal maturity (Schulz et al., 2016). Moreover, both brookite and anatase can grow to micron-sizes without being transformed to rutile (Parnell, 2004; Fuchs et al., 2015).

Early Cambrian black shales are widely distributed on the southeastern margin of the Yangtze platform, South China (Guo et al., 2007; Chen et al., 2015; Wen et al., 2015; Fig. 1). They formed under a variety of physicochemical conditions due to variable contributions of continental and biotic components with increasing water and burial depth, and they have been shown to contain relatively high V concentrations (e.g., Bao et al., 2012; Jiang et al., 2006; Wen et al., 2015). In this paper, we report on authigenic Ti-bearing minerals from two early Cambrian black shale successions in South China. They deposited on a continental shelf and in a slope-basin environment, respectively, and show contrasting morphologies and compositions. Results of this study provide new insights into the behavior of Ti in organic-rich sediments and a possible mechanism by which Ti can be mobilized and concentrated. We also discuss a possible re-distribution of redox sensitive elements in the black shales during their interaction with hydrocarbon liquids, and provide geochemical proxies for estimating redox conditions.

2 Geological setting

Late-Neoproterozoic to early Cambrian sedimentary successions are well preserved in the Yangtze Block and were deposited in the paleo-environmental settings

of a platform, a protected basin and the transitional belt between them (Fig.1). The earliest Cambrian rocks deposited in the basin, in order of increasing depth, were phosphorite/dolomite and black shale/chert. After a prolonged transgression, they were overlain by a thick succession of black shales. Black shales in the Meishucun section (N 24° 43′ 18.9″ E 102° 33′ 23.8″), Yunnan province, and in the Zhajin section (N 28° 57′ 05.2″ E 114° 12′ 48.7″), Jiangxi province were selected for this study (Figs. 1, 2a and 3a). Paleo-geographically, these two sections were located on a carbonate platform (Liu and Zhou, 2017; Wen et al., 2015) and in a transitional environment between the shelf and basin of the Yangtze platform, respectively (Fig. 1). Detailed descriptions of the regional geology are provided in Supplementary Note 1. Sixteen unaltered samples were collected from the Shiyantou Member in the Meishucun section and fourteen from the lower Wangyinpu Formation in the Zhajin section (see Supplementary Fig. S3). These two carbonaceous sedimentary sequences are stratigraphically correlative, and they both were deposited during Cambrian Stage1-2 (536 Ma-521 Ma) (see details in supplementary Note; Zhang et al., 2017, Wen et al., 2015; Gao et al., 2018).

3 Analytical methods

3.1 Scanning electron microscopy

Scanning electron microscope (SEM) examination was carried out at the Henan Province Rock and Mineral Testing Center, China, using a ZEISS MERLIN Compact

SEM equipped with an energy dispersive X-ray spectrometer (EDS), and back-scattered electron (BSE) detector. The Advanced Mineral Identification and Characterization System (AMICS) software package was used for the automated identification and quantification of minerals and synthetic phases. The acceleration voltage was 20 kV in BSE mode, which generated secondary electrons (SE_2) during imaging and EDS analyses. Based on petrographic observation under the SEM, the volume percent of major minerals, such as illite, quartz and biotite and titania were roughly estimated.

3.2 Electron probe microanalysis

Major element compositions of minerals were obtained using a JXA-8230 electron microprobe at the University of Hong Kong. The quantitative analyses were performed in wavelength dispersive mode (WDS) with an accelerating voltage of 15 kV, a specimen current of 2.0×10^{-8} A, and a beam diameter of 1 μm. The analytical uncertainties were less than 2%.

3.3 Laser Raman Spectroscopy

Titania minerals were analyzed using a Thermo Scientific DXR dispersive Raman microscope equipped with an Olympus M plan-BD 100X objective at the State Key Laboratory of Geological Processes and Mineral Resources, China University of Geosciences (Wuhan). The analytical conditions are described in Xiong et al. (2011). A laser beam with an output power of 24mW irradiated samples with a maximum power of 10 mW and an estimated spot size of 1 μm.

3.4 Transmission electron microscope (TEM)

Normally, samples for TEM imaging and analysis are mechanically polished to a thickness of a few micrometers and then milled to less than 1 μm in thickness using a 4.0 kV argon ion-beam on a GATAN precise ion polishing system. However, black shales were too soft to be milled properly. In view of this, the samples were ground to ~ 200 mesh and then, micron- and nano-size titania crystals for TEM analysis/imaging were selected using the SEM. The analyses were carried out at the Queen Mary Hospital, the University of Hong Kong, using a FEI Tecnai G2 20 S-TWIN scanning transmission electron microscope (dark field and bright field detectors with TIA acquisition software). The microscope is equipped with an INCAx-sight EDS Detector with INCA Energy TEM software, and Gatan image filtering system (749 1k × 1k camera system with digital/micrograph acquisition software).

3.5 Bulk rock trace element analyses

Samples analyzed in this study for their bulk composition were prepared by removing the surface rind with saw. They were then crushed with a steel jaw crusher, and powered using an aluminum oxide mill.

Bulk rock concentrations of trace elements, including REEs, were determined using a VG Plasma-Quad Excell inductively coupled plasma mass spectrometer (ICP-MS) at the Institute of Geochemistry, Chinese Academy of Sciences (CAS), Guiyang, China, after a two-day closed-beaker digestion using a mixture of HF and HNO_3 acids in high-pressure autoclaves (Qi et al., 2000). Pure elemental standard solutions were used for external calibration and BHVO-1 and SY-4 were used as reference materials.

149 The analyses were accurate to better than 5%.

150 **3.6 Total organic carbon content**

151 Total organic carbon (TOC) contents were measured using a Multi EA 4000
152 carbon/sulfur analyzer with a high temperature furnace and acidification module (Eltra,
153 Germany). Inorganic carbon (carbonate) was removed by adding 6 mol/L HCl to about
154 2 g of powdered shale. Approximately 100 mg of the solid residue was then weighed
155 into a ceramic boat and combusted in pure (99.95%) O_2 at 1350 °C for ~3 mins. The
156 analytical errors for TOC were ±0.2 wt% based on analysis of carbonate standard,
157 AR4007 (Alpha, USA).

158 3.7 Rock-Eval pyrolysis

159 Rock-Eval pyrolysis experiments were performed on an OGE-VI Hydrocarbon
160 Evaluation Work station at Yangtze University. Samples were progressively heated to
161 600 ℃ in a helium atmosphere. The measured parameters were S_1 (adsorbed free liquid
162 hydrocarbons) which was measured in an oven at a constant temperature of 300 ℃ for
163 3 min; and S_2 (residual petroleum potential), which was measured when samples were
164 heated from 300 to 600 ℃ at a rate of 25 C/min. PRO-3 with S_1=0.61 mg HC/ g rock
165 and S_2=4.10 mg HC/ g rock was used as a standard material. The uncertainties for S_1
166 and S_2 were <±5% based on analysis of the standard. The HI parameter (hydrogen
167 index) was calculated with following formula: $HI = 100*S_2/TOC$.

168 **3.8 Sm–Nd isotopic analyses**

169 Bulk rock Sm–Nd isotopic analyses were performed on a VG-354 thermal

ionization magnetic sector mass spectrometer at the Institute of Geochemistry, Guiyang, China. The chemical separation and isotopic measurement procedures are described in Zhang et al. (2001). Mass fractionation corrections for Nd isotopic ratios were performed assuming a $^{146}Nd/^{144}Nd$ ratio of 0.7219. The uncertainty in the Sm/Nd isotopic ratio was less than ± 0.5% (relative).

4 Petrography

4.1 Black shales in the Meishucun section

Black shales from the Meishucun section are finely laminated, and composed of mineral assemblages involving quartz aggregates, dolomite, pyrite, biotite, clay minerals and traces of amphibole (Fig. 2b). Quartz, dolomite and clay minerals comprise >80 vol% of the rocks (Fig. 2b). The quartz and dolomite grains are predominantly sub-angular to sub-rounded and range from 10 to 50 μm in diameter. There also contain minor proportions of biotite (3 vol%) and amphibole (<0.5 vol%) crystals that are generally 10 μm in width and 20-100 μm in length. They are partially altered to chlorite (Figs. 2b-g). The clay minerals are <2 μm in diameter, and occur in clusters in the interstices between quartz crystals or around biotite and amphibole crystals (Figs. 2e-g). Altered biotite crystals contain tabular brookite crystals (see below for how they were identified) and euhedral pyrite grains along their cleavages (Figs. 2c-g). Without exception, the brookite is restricted to biotite relicts, whereas pyrite is much more prevalent in the matrix, where it occurs as euhedral crystals, framboids or nodular aggregates, and generally ranges from 2 to 15 μm in diameter (Fig. 2h).

Authigenic phosphatic grains (colloidal nodules) are sparsely distributed and occupy less than 2 vol% of the rock (Fig. 2b).

4.2 Black shales in the Zhajin section

Black shales in the Zhajin section are variably layered, and in places display distinct submillimeter-scale parallel laminae or thin-thick beds (Fig. 3a). The samples are composed mainly of quartz, clay minerals, titania minerals, pyrite and bitumen (Figs. 3 and 4). Quartz and clay minerals, comprising >80 vol% of the rock, are typically less than 5 μm in diameter (Fig. 4). Disseminated anatase (see below for how it was identified) comprises up to 3 vol% of the rock and occurs as sponge-like aggregates of micron-size crystals (Figs. 3b-f). These aggregates commonly crystallized around sphalerite and range from 50 μm to 300 μm in diameter (Figs. 3c-f). Sphalerite is amorphous and porous. Bitumen (~3 vol%) is disseminated throughout the rock; it occupies interstices among sphalerite and titania mineral aggregates (Figs. 3 and 4). Authigenic quartz and clay minerals are enclosed in bitumen (Figs. 4c and d). The clay mineral crystals are sheet-like and <2 μm in diameter, and concentrated in the interstices among the quartz crystals (Figs. 3g and h). Pyrite occurs as framboids, euhedral crystals or pseudomorphs replacing animal fossils.

5 Chemical composition of crystalline and organic phases

5.1 Brookite/anatase

The titania minerals in biotite relics of black shales from the Meishucun section produced a sharp peak at ~153 cm^{-1} and low-intensity peaks at 127, 213, 247, 284, 327,

212 369, 456 and 544 cm^{-1}) on the Raman spectrum (Fig. 5a). These peaks correspond to
213 those for brookite in a direction parallel to XX (the 127, 153, 247 and 544 cm^{-1} peaks),
214 XY (the 213, 284 and 327 cm^{-1} peaks) and XZ (the 369 and 456 cm^{-1} peaks (Fig. 5a;
215 Iliev et al., 2013). All titania crystals in black shales from the Zhajin section produced
216 strong peaks at about 146, 396, 513 and 635 cm^{-1}. These wave numbers are diagnostic
217 of anatase (Fig. 5a; Frank et al., 2012). Transmitted electron microscopic analysis of
218 titania crystals from black shales of the Zhajin section yielded an electron diffraction
219 pattern for the $[\bar{1},\bar{1},1]$ plane, corresponding to d-spacings of 0.3595 nm $(1,0,\bar{1}1)$ and
220 0.3609 nm $(0,1,\bar{1})$ (Figs. 5b-d). These d-spacings, within the experimental error, are
221 the same as those for the $[\bar{1},\bar{1},1]$ plane of anatase (0.3516 nm) and confirm the Laser
222 Raman Spectroscopic identification (Fig. 5).

223 In order to further characterize the titania minerals, their chemical compositions
224 were determined using the electron microprobe (EMP). The EMP analytical data were
225 obtained from a spot with a diameter of 1 μm that correspond to an excitation volume
226 with a diameter of ~ 4 μm, which is larger than most of the analyzed mineral grains.
227 Therefore, the EMP data represent an average composition of numerous individual
228 nano-size crystals and possibly also non-titania mineral components. The valance of Fe
229 and V in the minerals were not determined and instead are reported as FeO and V_2O_3
230 concentrations. Brookite from the black shales of the Meishucun section has elevated
231 Al_2O_3 (0.43-3.9 wt%), SiO_2 (0.95-10 wt%) and FeO (0.74-3.6 wt%) contents, which
232 may reflect contamination from the surrounding clay minerals, and relatively low V_2O_3

(0.23-1.93 wt%) and TiO_2 (71-91 wt%) contents. In contrast, anatase from the black shales of the Zhajin section has high SiO_2 (0.36-5.3 wt%) and low Al_2O_3 (0.1-1.0 wt %) contents, suggesting that the contamination was mainly from quartz that filled interstices within the anatase aggregates. The anatase has a FeO content from 0.47 to 1.4 wt%, a V_2O_3 content from 3.4 to 5.4 wt% and a TiO_2 content from 75 to 93 wt% (Fig. 6; Table 1).

5.2 Phyllosilicate minerals

Biotite crystals in the black shales from the Meishucun section have low SiO_2 contents, ranging from 30 wt% to 36.2 wt%, and high FeO (17-20 wt%) and TiO_2 (>0.23 wt%) contents, whereas the clay minerals have high SiO_2 (45-57 wt%) and Al^{VI} (2.4~3.9 apfu) contents (Figs. 7a and b). The small clay mineral crystals are compositionally similar to the large muscovite crystals (Table 2). They have relatively high Fe/Fe+Al ratios and moderate K contents, consistent with Al-rich mixed layer illite - smectite (I/S), smectite or Fe-rich I/S (Fig. 7b). All the clay minerals in the black shales of the Meishucun section have low V_2O_3 (<0.2 wt%) and Cr_2O_3 (<0.14) contents.

Clay minerals in the black shales of the Zhajin section have low Fe/Fe+Al ratios and variable K contents, indicating that they comprise kaolinite, Al-rich I/S and illite (Fig. 7b). Vanadium is negatively correlated with Al^{VI} in the clays (Figs. 7c). Most of the clay minerals have high V_2O_3 (ca. 2.5 wt%) and low TiO_2 (0.22 wt%) contents; V_2O_3 and TiO_2 contents display a positive correlation, except for minerals with a very low V_2O_3 content (Figs. 7d).

5.3 Organic phases

Black shales of the Meishucun section have much lower TOC contents (1 to 4 wt%) than those of the Zhajin section (7 to 15 wt%) (Table 4; Fig. 8). However, they yielded higher S_1 (0.04-0.24 mg HC/ g rock), S_2 (0.1-0.43 mg HC/ g rock) and HI (3.8-20 mg HC/ g TOC) values than the black shales of the Zhajin section, which yielded the following values S_1=0.01-0.14 mg HC/ g rock, S_2=0.01-0.29 mg HC/ g rock and HI=0.1-2.0 mg HC/ g TOC. Forty energy dispersive X-ray spectroscopic and 14 EPM spot analyses of the bitumen aggregates yielded large peaks for carbon and oxygen and small peaks for Si, Al, S, K, Ti, V, Fe and Zn (Table 3 and supplementary Table A1).

6 Bulk rock compositions

Black shales from the Meishucun section have high Ti (5205 ppm on average) and low V (98-555 ppm) contents. They also have high Sc (13.8-17.4 ppm), Co (9.8-17.5 ppm) and Th (5.9-11 ppm) contents and low Cr (60-781 ppm), Ni (39-86 ppm) and U (4.4-15.8 ppm) contents. By comparison, black shales in the Zhajin section have over an order of magnitude higher V (2900-11000 ppm), and much higher Cr (125-1221 ppm), Ni (41-294 ppm) and U (28-663 ppm) contents than black shales from the Meishucun section. However, they have significantly lower Ti (1830 ppm on average), Sc (4-16 ppm), Co (0.4-15.4 ppm) and Th (3.1-6.5 ppm) contents. Barium is highly enriched in Ba-feldspar-rich layers in black shales from the Zhajin section. Black shales from both sections have low εNd(t) values (~-20; Table 5), although a relatively high εNd(t) value (-12) was obtained from a shale at the top of the Zhajin section.

7 Discussion

7.1 Derivation of Ti from detrital components

Detrital titania minerals are rarely observed in marine sediments owing to their high density (3.8~4.3g/cm^3), which impedes their transport into marine basins (Schulz et al., 2016). Wherever these minerals are present, they are either rounded in shape (Baioumy, 2014) or show signs of partial dissolution (Schulz et al., 2016). In contrast, brookite in black shales of the Meishucun section occurs as tabular crystals along cleavages of biotite (Fig. 2c), and anatase in black shales of the Zhajin section forms sponge-like crystal aggregates and is intergrown with sphalerite (Fig. 3c). These observations imply that the titania minerals (brookite and anatase) in the Meishucun and Zhajin black shales are authigenic.

Vertical redox changes and remineralization of organic matter in the water column are two widely invoked mechanisms for producing trace element-rich authigenic minerals in sediments (Algeo and Maynard, 2004; Emerson and Huested, 1991; Gregory et al., 2017; Jones and Manning, 1994). During the deposition of black shales, accumulation and subsequent decay of organisms along and below the water-sediment interface consumes the O_2 of the bottom water, generating a stratified redox state in the basin (Kristensen, 2000). Redox sensitive elements, such as V, Mo and Cr have relatively high solubility under oxic conditions and are insoluble in reduced environments. They are thus precipitated and accumulated in black shales (Algeo and Maynard, 2004). However, Ti is inert to the redox change in seawater. It has a low

296 solubility under both oxic and anoxic conditions in its dominant valance state (4+),
297 which explains its extremely low concentration in open seawater (0.005 to 0.35nM; Van
298 Den Berg et al., 1994; Skrabal, 2006). Organisms have the ability to extract elements
299 (e.g., V and P) from seawater and release them to form authigenic minerals after burial,
300 even if the elements are present in very low concentrations (e.g., Algeo and Maynard,
301 2004; Yu and Wang, 2004). Unfortunately, Ti is not an essential element for life, and
302 thus cannot be accumulated biologically as authigenic titania minerals.

303 Titanium-bearing minerals, such as biotite and amphibole, can be carried as
304 detritus into oceans, and subsequently accumulate in fine-grained clastic sediments. It
305 is possible that authigenic titania minerals form from these minerals, particularly from
306 igneous and metamorphic biotite, which may contain several weight percent of TiO_2
307 (Henry and Guidott, 2002). Indeed, this would be the case for black shales of the
308 Meishucum section, in which the only authigenic titania mineral, brookite, occurs
309 exclusively along cleavages in relics of detrital biotite (Figs. 2c-g). Based on the
310 association of brookite with illite or illite-smectite and biotite relicts, we propose that
311 biotite decomposed to form clay minerals during diagenesis, thereby releasing Ti,
312 which was then incorporated into brookite.

313 **7.2 The bitumen-anatase association**

314 In contrast to the Meishucum section, relicts of biotite or any other detrital Ti-
315 bearing minerals are not observed in black shales from the Zhajin section. However,
316 bitumen, which formed during hydrocarbon generation and solidification, is an

317 important phase in black shales from the Zhajin section and is closely associated with
318 anatase. Furthermore, the bitumen contains appreciable Ti (up to 1 wt%; Table 3 and
319 supplementary Table A1). It is thus reasonable to argue that hydrocarbon liquids
320 released during diagenesis played a key role in the transport and deposition of Ti. Fuchs
321 et al. (2015) noted that anatase nano-crystals in the Witwatersrand Carbon Leader Reef
322 occur within bitumen masses rather than along their borders, consistent with their
323 precipitation from liquid hydrocarbons. By contrast, in the Zhajin section, anatase
324 concentrated either around or inter-mingled with bitumen, arguing against dissolution
325 and transport of Ti in a hydrocarbon liquid.

326 Anatase and bitumen have also been reported to occur at the oil-water interface in
327 an oil field (Schulz et al., 2016). Oil-water interfaces are locations of very low pH (<3
328 - 7) in the aqueous phase due to the anaerobic degradation of the oil and the resulting
329 production of methane, carbon dioxide and acetic acid (Schulz et al., 2016). Aqueous
330 fluids at such interfaces could be very effective in dissolving Ti-minerals in the host
331 shales by forming stable Ti-organic complexes. Low pH and the anaerobic degradation
332 of the oil would also promote formation and aggregation of nano-crystal titania (Chen
333 et al., 2012; Schulz et al., 2016). However, owing to the very low porosity of black
334 shales, it is difficult to envisage a large-scale migration of oil and water and the
335 formation of an oil-water interface in such rocks.

336 On the other hand, the release of diagenetic acids such as acetic or oxalic acid
337 during the formation of hydrocarbons would decrease pore-water pH, generating a

micro-environment that is favorable for the dissolution of Ti-bearing minerals (Schulz et al., 2016). The organic acids could also form chelation complexes with Ti^{4+}, which promotes migration of Ti in pore waters. In the Zhajin section, anatase occur as sponge-like aggregates, which likely precipitated in pore water cavities. It is thus possible that low-pH pore water with abundant organic acids released during diagenesis played a key role in the dissolution and transport of Ti.

Titanium could also have been transported by and deposited from an acidic low temperature hydrothermal fluid that interacted with the shales after diagenesis (Parnell, 2004). Because Nd isotopes do not fractionate, even at low temperature (Ling et al., 1997), and the oceanic residence time of Nd (300~1000 year) is less than the oceanic mixing time (1500 ~2000 years) (Tachikawa et al., 2003), Nd isotopes can be used to determine whether rocks have undergone modification by post-diagenetic hydrothermal fluids. Black shales in the Meishucun and Zhajin sections have relatively constant εNd(t) values (mostly between -19.7 and -18.8), which are indicative of stable continental inputs with no involvement of hydrothermal fluids (Table 5). An exception is a sample collected at top of the Zhajin section that has a relatively high εNd(t) value of -12, which may reflect prolonged interaction with meteoric water. We therefore conclude that anatase in the Zhajin section formed as a result of dissolution and transportation by hydrocarbons during late-diagenesis.

7.3 Growth of titania minerals

7.3.1 Precipitation of brookite and anatase

359 Brookite in black shales from the Meishucun section occurs along cleavages of
360 partially decomposed detrital biotite crystals (Fig. 2). Given the very low solubility of
361 Ti in aqueous fluids and the preferential adsorption of metal oxides (Cornu et al., 1999),
362 Ti was predictably immobile and crystallized in situ in black shales of the Meishucun
363 section. In contrast, Ti in the Zhajin black shales was likely mobilized by the formation
364 of stable organic complexes. Precipitation of anatase nano-crystals is inferred to have
365 resulted from a subsequent increase in pH, which destabilized the organic Ti complexes;
366 a temperature increase may also have been a contributing factor by destroying essential
367 organic ligands (Schulz et al., 2016). Increasing pH was also likely responsible for the
368 observed aggregation of the nano-crystals, on the basis of the experimental results
369 showing that adsorption of humic acids by nano-crystals of TiO_2 strongly decreases
370 above pH values of 5 to 6, and that this decrease promotes anatase aggregation (Yang
371 et al., 2009).

372 As discussed above, titania mineralization in the Zhajin section involved a role for
373 liquid hydrocarbons, the genetration of which depended on the thermal maturity and
374 TOC content of the black shales. The assessment of thermal maturity in pre-Devonian
375 shales is challenging due to the absence of vitrinite macerals that precludes the
376 application of vitrinite reflectance petrography, the most-widely used assessment
377 technique (c.f. Cheshire et al., 2017). We therefore compared the thermal maturity of
378 the Meishucun and Zhajin sections using Rock-Eval pyrolysis data. As is the case with
379 most Cambrian shales, black shales from the Zhajin section have very low residual

petroleum potential (S_2=0.01-0.29 mg HC/ g rock) but a very high TOC content (7 to 15 wt%). The extremely low HI values (0.1-2.0 mg HC/ g TOC) for this section indicate that the black shales have a very high thermal maturity and released abundant hydrocarbons during burial and late-diagenesis. In contract, black shales from the Meishucun section have a little higher S_2 value (0.1-0.43 mg HC/ g rock) and much lower TOC (1 to 4 wt%) than the black shales of the Zhajin section. The high HI values (3.8-20 mg HC/ g TOC) indicate that the Zhajin black shales have lower thermal maturity and still retain the potential for hydrocarbon generation. Also, the higher TOC content led to the formation relatively large pores and higher overall porosity during cracking, which accelerated the migration of Ti. The clay mineral in the black shales from the Zhajin section has a much lower Fe/Al ratio, and is much closer in composition to illite in composition than the clay mineral in black shales from the Meishucun section (Fig. 7b). In addition, V and Al^{VI}, and Cr and Al^{VI} are negatively correlated (Fig. 7c; Table 2), indicating the substitution of Cr and V for Al during the smectite-illite transition. This is consistent with the deeper burial depth and a higher degree of hydrocarbon maturation of the Zhajin black shales relative to the Meishucun black shales.

Thus, we propose that, in both sections, detrital biotite was the main source of Ti and partially decomposed during early diagenesis, forming tabular authigenic brookite crystals within the relict grains. In the Zhajin black shales, however, the greater maturity of the organic matter and high TOC content led to the generation of liquid

401 hydrocarbons, which interacted locally with pore waters reducing their pH, thereby
402 destroying the relict biotite grains and enabling mobilization of the authigenic brookite
403 (and Ti in the biotite) as aqueous organic Ti complexes. These complexes, as discussed
404 above, were subsequently destabilized to form anatase nano-crystals and, in turn,
405 sponge-like aggregates of anatase nano-crystals.

406 **7.3.2 Controls on crystallization of brookite and anatase**

407 According to Schulz et al. (2016), anatase is the first titania phase to crystallize
408 from aqueous solutions (as nano-crystals) as its surface energy is lower than that of
409 brookite. However, it can be readily converted to brookite during growth. One of the
410 mechanisms is the nucleation of brookite from the twin planes of anatase, which has a
411 similar structure to that of brookite (Zhang and Banfield, 2014). In sol-gel experiments
412 designed to synthesize nano-crystalline TiO_2, anatase is the dominant phase if the
413 crystals are <11 nm in diameter, whereas brookite dominates when the crystals are
414 between 11 and 35 nm in diameter and rutile forms when the crystal size is >35nm
415 (Zhang and Banfield, 2014). However, micron-size crystals of both anatase and
416 brookite are observed in black shales (Cabral et al., 2012; Parnell, 2004; Schulz et al.,
417 2016). It has therefore been suggested that, in natural environments, the stability and
418 growth of titania are mainly controlled by pH, with brookite formation favored at
419 moderately acidic pH (3-6) and anatase at high pH (>5) (Zhang and Banfield, 2014).
420 These findings are consistent with the observation that brookite in the Meishucun
421 section crystallized in a micro-environment with abundant HS^- (acidic), and anatase

422 precipitated rapidly in black shales of the Zhajin section after destabilization of organo-
423 Ti complexes as pH increased to a near neutral value.

424 Dopants in the titania change its lattice and thus can lead to the formation of
425 different phases. For example, in sol-gel syntheses of titania, it has been observed that
426 elevated concentrations of Mo^{6+} lead to the transformation of brookite to anatase,
427 whereas high concentrations of Fe^{3+} and V^{5+} favor the formation of brookite (Khan and
428 Berk, 2014). In contrast, it has been shown that incorporation of V^{4+} leads to preferential
429 formation of anatase (Li et al., 2010). Although these two studies were undertaken at
430 different temperatures (300°C/500°C and 50°C, respectively) using different inorganic
431 Ti precursors (Ti oxysulfate vs. tetrabutyl titanate), the results suggest that the
432 incorporation of V with lower valance in the second study may be the reason for the
433 formation of anatase rather than brookite (Li et al., 2010).

434 In our study, both brookite in black shales from Meishucun and anatase in black
435 shales from Zhajin contain abundant vanadium (>1 wt% V_2O_3). As discussed above,
436 brookite in the Meishucun black shales precipitated within pore water, whereas the
437 formation of anatase in black shales from Zhajin was closely linked to the generation
438 of organic-rich liquids after burial. Significantly, V in crude oils occurs mainly as V^{4+}
439 (Baranova and Fortunatov, 2012; Mandal et al., 2014; Zhang et al., 2014), which may
440 be a reason why anatase was favored over brookite in black shales from Zhajin. By
441 analogy, it is therefore possible that V in black shales from Meishucun was mostly
442 present as V^{5+}, thereby favoring the precipitation of brookite. Thus, a different pH

443 and/or valance state of V may be the reason that authigenic titania occurs as brookite in
444 the Meishucun black shales and as anatase in the Zhajin black shales.

445 **7.4 Implications for the reliability of redox proxies**

446 The geochemistry of marine black shales, including the concentration of redox
447 sensitive elements (RSEs; e.g., Mo, U and V), the ratios of V/V+Ni and the Fe
448 speciation, have long been taken as important proxies for paleo-environmental
449 conditions (e.g., Algeo and Maynard, 2004; Anderson and Raiswell, 2004; Tribovillard
450 et al., 2006). Recent studies, however, have demonstrated that multiple geochemical
451 proxies may yield conflicting redox interpretations. For example, early Ediacaran black
452 shales from the Yanjia section have highly variable Fe speciation and enrichment of
453 RSEs, suggesting that redox conditions varied from oxic to euxinic, whereas their
454 persistently high TOC/P ratios argue for an anoxic dominated depositional environment
455 (Jin et al., 2018). Similarly, Early Cambrian black shales from the Hetang Formation
456 have high but variable RSEs/TOC ratios, which are indictive of a euxinic depositional
457 environment but conflict with the presence of oxygen-dependent sponge species in the
458 shales (Cheng et al., 2017). Although the high variability in the values of geochemical
459 redox proxies have been attributed to transient redox changes (Cheng et al., 2017), or
460 different sensitivities of the elements to high-frequency redox fluctuations (Jin et al.,
461 2018), the driving forces for the transient or high-frequency redox changes are unclear.

462 The mobilization of the normally inert element, Ti, the Zhajin black shales is
463 evidence that trace element re-distribution during late-diagenesis may be common.

464 Indeed, some redox sensitive or environmentally toxic elements, including V, Ni, Fe,
465 Cr, Zn, Mo and Hg, have been shown to be re-distribute as a result of their concentration
466 in the organic fraction at conditions of high thermal maturity (de Souza et al., 2006;
467 Fein and Williams-Jones, 1997). For example, bitumen in black shales from the La
468 Luna Formation, Maracaibo Basin has a high V concentration (up to 1730 ppm) and a
469 higher V/V+Ni ratio than its host rocks (Lo Monaco et al., 2002). Similarly, Fe
470 concentrations in crude oils and their condensates from South African Basins can be as
471 high as 7300 ppm (Akinlua et al., 2015). The affinity of organic phases for these metals
472 indicates that, as is the case for Ti, they are readily mobilized when hydrocarbon-rich
473 liquids are generated in the sediments.

474 Owing to the extremely low permeability of black shales, liquid hydrocarbon
475 migration is spatially limited (Gao et al., 2018). Thus, although sedimentary sequences
476 likely exhibit increased variability in the contents of RSEs after they have interacted
477 with hydrocarbon-rich liquids, this increase may be relatively small. A more significant
478 effect of the interaction of these sequences with hydrocarbon liquids is the release of
479 highly reactive Fe into the liquids through the dissolution of detritus, e.g., biotite (Figs.
480 3c and 3e), which could change the bulk-rock Fe speciation. Nonetheless, because
481 hydrocarbon liquids cannot migrate far in shales due to the low-porosity of the latter,
482 the average contents of RSEs of these rocks, if established with high-resolution
483 sampling, are likely to record relatively reliable redox information. For this reason, our
484 overarching conclusion for the black shales considered in this study, which was reached

by considering the various redox proxies jointly, is that black shales in the Meishucun section formed under oxic-dysoxic conditions, whereas the Zhajin black shales were deposited in an anoxic environment (Fig. 8a; Hatch and Leventhal, 1992; Jones and Manning, 1994). In summary, although it appears that the above proxies can be applied reliably to estimate redox conditions for high thermal maturity black shales, this may not be the case for shales in which there are transient or high-frequency changes in the concentrations of RSEs and Fe species.

8 Conclusions

Detrital biotite was the major source of Ti for the authigenic titania in early Cambrian black shales, South China. During early diagenesis, Ti in black shales was immobile and precipitated in situ as brookite. However, the generation of hydrocarbon liquids can lead to complete destruction of the Ti-bearing detritus and the mobilization of Ti from brookite due to the formation of stable organic-Ti complexes. These liquids precipitated nano-crystalline anatase and eventually nanocrystalline anatase aggregates in response to increasing pH. Because of the high solubility of vanadium in liquid hydrocarbons, this also led to the incorporation of V^{4+} in the anatase structure. Our study illustrates the role that liquid hydrocarbons play in the mobilizarion of Ti in black shales. Finally, the study emphasizes the need to consider the possibility that many elements used as redox proxies may be re-distributed in organic rich shales during late-diagenesis, which could potential render them unreliable.

Acknowledgements

This research was supported financially by grants from the Research Council of Hong Kong (17306814), the National Nature Science Foundation of China (41572170 and 41772087), the "CAS Hundred Talents" Project to J.F. Gao and an HKU Visiting Professorship to Williams-Jones. We thank Dr. Wen Zhao for his assistance in the field and Prof. Liang Qi for the trace element analysis. We appreciate the constructive comments from the journal editor (Prof. Karen Johannesson) and three reviewers (Dr. Junpeng Zhang, Dr. Arkadiusz Derkowski and an anonymous reviewer) that helped improve the paper.

References

Algeo, T.J., Maynard, J.B., 2004. Trace-element behavior and redox facies in core shales of Upper Pennsylvanian Kansas-type cyclothems. Chemical Geology, 206 (3-4): 289-318.

Akinlua, A., Sigedle, A., Buthelezi, T., Fadipe, O.A., 2015. Trace element geochemistry of crude oils and condensates from South African Basins. Marine and Petroleum Geology, 59: 286-293.

Baioumy, H.M., 2014. Ti-bearing minerals in sedimentary kaolin deposits of Egypt. Applied Clay Science, 101: 345-353.

Bao, S., Zhang, Y., Hang, J., Yang, X., Hu, Y., 2012. Determination of vanadium valency in roasted stone coal by separate dissolve-potentiometric titration

method, MRS Proceedings. Cambridge Univ Press, pp. imrc2011-1380-s21-full013.

Baranova, V.N., Fortunatov, A.V., 2012. Vanadium: chemical properties, uses and environmental effects. Chemical Engineering Methods and Technology. Nova Science Pub Inc.

Byrne, C., Fagan, R., Hinder, S., McCormack, D.E., Pillai, S.C., 2016. New approach of modifying the anatase to rutile transition temperature in TiO_2 photocatalysts. RSC Advances, 6 (97): 95232-95238.

Cabral, A.R. et al., 2012. Anatase nanoparticles on supergene platinum-palladium aggregates from Brazil: titanium mobility in natural waters. Chemical Geology, 334: 182-188.

Cheng, M. et al., 2017. Transient deep-water oxygenation in the early Cambrian Nanhua Basin, South China. Geochimica Et Cosmochimica Acta, 210: 42-58.

Cheshire, S. et al., 2017. Assessing thermal maturity beyond the reaches of vitrinite reflectance and Rock-Eval pyrolysis: a case study from the Silurian Qusaiba formation. International Journal of Coal Geology, 180: 29-45.

Chen, G.X., Liu, X.Y., Su, C.M., 2012. Distinct effects of humic acid on transport and retention of TiO_2 rutile nanoparticles in saturated sand columns. Environmental Science & Technology, 46 (13): 7142-7150.

Cornu, S. et al., 1999. Evidence of titanium mobility in soil profiles, Manaus, central Amazonia. Geoderma, 91 (3-4): 281-295.

548 de Souza, R.M., Meliande, A.L.S., da Silveira, C.L.P., Aucelio, R.Q., 2006.
549 Determination of Mo, Zn, Cd, Ti, NiVFe, Mn, Cr and Co in crude oil using
550 inductively coupled plasma optical emission spectrometry and sample
551 introduction as detergentless microemulsions. Microchemical Journal, 82 (2):
552 137-141.
553 Emerson, S.R., Huested, S.S., 1991. Ocean anoxia and the concentrations of
554 molybdenum and vanadium in Seawater. Marine Chemistry, 34 (3-4): 177-196.
555 Fein, J.B., Williams-Jones, A., 1997. The role of mercury-organic interactions in the
556 hydrothermal transport of mercury. Economic Geology, 92(1): 20-28.
557 Frank, O. et al., 2012. Raman spectra of titanium dioxide (anatase, rutile) with identified
558 oxygen isotopes (16,17,18). Physical Chemistry Chemical Physics, 14 (42):
559 14567-14572.
560 Fuchs, S., Schumann, D., Williams-Jones, A.E., Vali, H., 2015. The growth and
561 concentration of uranium and titanium minerals in hydrocarbons of the Carbon
562 Leader Reef, Witwatersrand Supergroup, South Africa. Chemical Geology, 393-
563 394: 55-66.
564 Gao, F. et al., 2018. Pore characteristics and dominant controlling factors of overmature
565 shales: A case study of the Wangyinpu and Guanyintang Formations in the
566 Jiangxi Xiuwu Basin. Interpretation, 6 (2): T393-T412.
567 Gregory, D.D. et al., 2017. Whole rock and discrete pyrite geochemistry as
568 complementary tracers of ancient ocean chemistry: An example from the

569 Neoproterozoic Doushantuo Formation, China. Geochimica Et Cosmochimica
570 Acta, 216: 201-220.
571 Guo, Q.J. et al., 2007. Trace element chemostratigraphy of two Ediacaran-Cambrian
572 successions in South China: implications for organosedimentary metal
573 enrichment and silicification in the early Cambrian. Palaeogeography
574 Palaeoclimatology Palaeoecology, 254 (1-2): 194-216.
575 Hatch, J.R., Leventhal, J.S., 1992. Relationship between inferred redox potential of the
576 depositional environment and geochemistry of the upper pennsylvanian
577 (Missourian) Stark shale Member of the Dennis Limestone, Wabaunsee
578 Country, Kansas, USA. Chemical Geology, 99 (1-3): 65-82.
579 Henry, D.J., Guidott, C.V., 2002. Titanium in biotite from metapelitic rocks:
580 Temperature effects, crystal-chemical controls, and petrologic applications.
581 American Mineralogist, 87(4): 375-382.
582 Iliev, M.N., Hadjiev, V.G., Litvinchuk, A.P., 2013. Raman and infrared spectra of
583 brookite (TiO2): Experiment and theory. Vibrational Spectroscopy, 64: 148-
584 152.
585 Jiang, S.Y. et al., 2006. Trace-and rare-earth element geochemistry and Pb–Pb dating
586 of black shales and intercalated Ni–Mo–PGE–Au sulfide ores in Lower
587 Cambrian strata, Yangtze Platform, South China. Mineralium Deposita, 41(5):
588 453-467.
589 Jin, C.S. et al., 2018. Highly heterogeneous "poikiloredox" conditions in the early

590 Ediacaran Yangtze Sea. Precambrian Research, 311: 157-166.
591 Jones, B., Manning, D.A.C., 1994. Comparison of geochemical indexes used for the
592 interpretation of palaeoredox conditions in ancient mudstones. Chemical
593 Geology, 111(1-4): 111-129.
594 Khan, H., Berk, D., 2014. Synthesis, physicochemical properties and visible light
595 photocatalytic studies of molybdenum, iron and vanadium doped titanium
596 dioxide. Reaction Kinetics Mechanisms and Catalysis, 111(1): 393-414.
597 Kim, J., Dong, H.L., Seabaugh, J., Newell, S.W., Eberl, D.D., 2004. Role of microbes
598 in the smectite-to-illite reaction. Science, 303(5659): 830-832.
599 Kristensen, E., 2000. Organic matter diagenesis at the oxic/anoxic interface in coastal
600 marine sediments, with emphasis on the role of burrowing animals.
601 Hydrobiologia, 426(1-3): 1-24.
602 Li, H., Zhao, G.L., Chen, Z.J., Han, G.R., Song, B., 2010. Low temperature synthesis
603 of visible light-driven vanadium doped titania photocatalyst. Journal of Colloid
604 and Interface Science, 344(2): 247-250.
605 Ling, H.F. et al., 1997. Evolution of Nd and Pb isotopes in Central Pacific seawater
606 from ferromanganese crusts. Earth and Planetary Science Letters, 146(1-2): 1-
607 12.
608 Liu, Z.-R.R., Zhou, M.-F., 2017. Meishucun phosphorite succession (SW China)
609 records redox changes of the early Cambrian ocean. GSA Bulletin, 129 (11-12):
610 1554-1567.

611 Lo Monaco, S. et al., 2002. Distribution of major and trace elements in La Luna
612 formation, southwestern Venezuelan basin. Organic Geochemistry, 33(12):
613 1593-1608.
614 Mandal, P.C., Goto, M., Sasaki, M., 2014. Removal of Nickel and Vanadium from
615 Heavy Oils Using Supercritical Water. Journal of the Japan Petroleum Institute,
616 57 (1): 18-28.
617 Parnell, J., 2004. Titanium mobilization by hydrocarbon fluids related to sill intrusion
618 in a sedimentary sequence, Scotland. Ore Geology Reviews, 24 (1-2): 155-167.
619 Qi, L., Hu, J., Gregoire, D.C., 2000. Determination of trace elements in granites by
620 inductively coupled plasma mass spectrometry. Talanta, 51 (3): 507-513.
621 Ruiz Cruz, M., 2007. Genesis and evolution of the kaolin-group minerals during the
622 diagenesis and the beginning of metamorphism. Diagenesis and Low-
623 Temperature Metamorphism. Theory, Methods and Regional Aspects
624 Seminarios SEM, 3: 41-52.
625 Schulz, H.-M., Wirth, R., Schreiber, A., 2016. Nano-crystal formation of TiO2
626 polymorphs brookite and anatase due to organic—inorganic rock–fluid
627 interactions. Journal of Sedimentary Research, 86 (2): 59-72.
628 Skrabal, S.A., 2006. Dissolved titanium distributions in the Mid-Atlantic Bight. Marine
629 Chemistry, 102 (3-4): 218-229.
630 Steiner, M., Wallis, E., Erdtmann, B.D., Zhao, Y.L., Yang, R.D., 2001. Submarine-
631 hydrothermal exhalative ore layers in black shales from South China and

associated fossils - insights into a Lower Cambrian facies and bio-evolution. Palaeogeography Palaeoclimatology Palaeoecology, 169 (3-4): 165-191.

Tachikawa, K., Athias, V., Jeandel, C., 2003. Neodymium budget in the modern ocean and paleo-oceanographic implications. Journal of Geophysical Research-Oceans, 108 (C8): 3254.

Tribovillard, N., Algeo, T.J., Lyons, T., Riboulleau, A., 2006. Trace metals as paleoredox and paleoproductivity proxies: an update. Chemical Geology, 232(1-2): 12-32.

Van Den Berg, C.M.G., Boussemart, M., Yokoi, K., Prartono, T., Campos, M.L.A.M., 1994. Speciation of aluminum, chromium and titanium in the NW Mediterranean. Marine Chemistry, 45 (4): 267-282.

Velde, B.B., Meunier, A., 2008. The origin of clay minerals in soils and weathered rocks. Springer Science & Business Media, 1-405.

Wen, H.J. et al., 2011. Molybdenum isotopic records across the Precambrian-Cambrian boundary. Geology, 39 (8): 775-778.

Wen, H.J., Fan, H.F., Zhang, Y.X., Cloquet, C., Carignan, J., 2015. Reconstruction of early Cambrian ocean chemistry from Mo isotopes. Geochimica Et Cosmochimica Acta, 164: 1-16.

Xiong, Q., Zheng, J., Griffin, W.L., O'Reilly, S.Y., Zhao, J., 2011. Zircons in the Shenglikou ultrahigh-pressure garnet peridotite massif and its country rocks from the North Qaidam terrane (western China): Meso-Neoproterozoic crust–

653 mantle coupling and early Paleozoic convergent plate-margin processes.
654 Precambrian Research, 187 (1): 33-57.
655 Yang, K., Lin, D.H., Xing, B.S., 2009. Interactions of humic acid with nanosized
656 inorganic oxides. Langmuir, 25 (6): 3571-3576.
657 Yin, L., Li, J., Tian, H., Long, X., 2018. Rhenium–osmium and molybdenum isotope
658 systematics of black shales from the Lower Cambrian Niutitang Formation, SW
659 China: Evidence of a well oxygenated ocean at ca. 520 Ma. Chemical Geology,
660 499: 26-42.
661 Young, G.M., Nesbitt, H.W., 1998. Processes controlling the distribution of Ti and Al
662 in weathering profiles, siliciclastic sediments and sedimentary rocks. Journal of
663 Sedimentary Research, 68 (3): 448-455.
664 Yu, R.Q., Wang, W.X., 2004. Biological uptake of Cd, Se(IV) and Zn by
665 Chlamydomonas reinhardtii in response to different phosphate and nitrate
666 additions. Aquatic Microbial Ecology, 35 (2): 163-173.
667 Zhang, H. et al., 2001. Moderately depleted lithospheric mantle underneath the Yangtze
668 Block: evidence from a garnet lherzolite xenolith in the Dahongshan kimberlite.
669 Geochemical Journal, 35: 315-331.
670 Zhang, H.Z., Banfield, J.F., 2014. Structural Characteristics and Mechanical and
671 Thermodynamic Properties of Nanocrystalline TiO_2. Chemical Reviews, 114
672 (19): 9613-9644.
673 Zhang, Y. et al., 2017. Marine redox stratification during the early Cambrian (ca. 529-

509 Ma) and its control on the development of organic-rich shales in Yangtze Platform. Geochemistry, Geophysics, Geosystems, 18(6): 2354-2369

677 Figure captions

678

679 Figure 1. A simplified paleogeographic map of the Yangtze platform during the
680 Ediacaran-Cambrian transition, showing the four major facies under consideration
681 (modified from (Steiner et al., 2001; Zhang et al., 2017)).

682

683 Figure 2. Photograph (a), backscattered electron (BSE) (b and h) and secondary electron
684 (SE_2) (c-g) images of the black shale in the Meishucun section. a) the black shale
685 profile; b) the mineral distribution in a thin section cut oblique to the bedding plane;
686 the mineral distribution was determined using AMICS software; c) tabular brookite
687 crystals and pyrite along cleavages in a biotite relict; d) biotite grains replaced by nano-
688 crystalline aggregates of clay minerals; e) and f) authigenic clay minerals in the
689 interstices between detrital grains; g) directional alignment of biotite; h) pyrite
690 framboids and euhedral pyrite. *Q+C = quartz + trace clay mineral; Qtz = quartz; Fra=*
691 *Francolite; Chl = chlorite; Cl = clay minerals; Py = pyrite; Bio = biotite; Brk =*
692 *brookite Am = amphibole; Dol = dolomite; Un = undermined mineral or holes or*
693 *organic matter or bitumen.*

694

695 Figure 3. Photograph (a), BSE (b-d, g and h) and SE_2 (e and f) images of black shales
696 in the Zhajin section, Xiuwu area. a) the black shales profile; b) disseminated anatase
697 and bitumen; c) sponge-like anatase, and sphalerite intergrown with bitumen; d) the

mineral distribution determined using the AMICS software; anatase coated Fe-oxide; e) and f) the association of bitumen, sphalerite and anatase; g) and h) clay minerals. *Ana = anatase; Un = undermined mineral or holes or organic matters; Bt = Bitumen*

Figure 4. Secondary electron (a-d) and BSE (e and f) images of the black shale in the Zhajin section, Xiuwu area. a) and b) bitumen filling pores in the black shales; c) quartz fragments in bitumen; d) clay mineral in contact with bitumen.

Figure 5. Raman shift and a TEM image of titania minerals from black shales of the Meishucun and Zhajin sections, South China. a) Raman shift diagram, the red lines illustrate our spectra and the black line the spectra presented in (Iliev et al., 2013); b) bright field TEM images of anatase crystals from the Zhajin section; c) enlargement of the area labeled "c" in (b), showing individual anatase crystals; d) electron diffraction pattern for the [1,1,1] plane of anatase.

Figure 6. Binary diagrams illustrating compositional data for the titania minerals.

Figure 7. Binary diagrams illustrating compositional data for the phyllosilicate minerals. In a) bio=biotite and chl= chlorite; the shaded areas in b) indicate the fields of illite (il); smectite (sm); Al-rich illite - smectite mixed layer mineral (I/S_{Al}); Fe-rich illite - smectite mixed layer mineral (I/S_{Fe}); and glauconite (Gla).

719

720 Figure 8. Plots showing the depositional redox states of the Meishucun and Zhajin black

721 shales based on proxies involving vanadium: a) bulk rock V/V+NI vs. V/Cr; and b)

722 U/Th vs. Ni/Co of the black shales. *WR=whole rock.*

Liu, Z.-R.R., Zhou, M.-F., Williams-Jones, A.E., Wang, W., Gao, J.-F., 2019.
Diagenetic mobilization of Ti and formation of brookite/anatase in early Cambrian black shales, South China.
Chemical Geology, 506: 79-96.

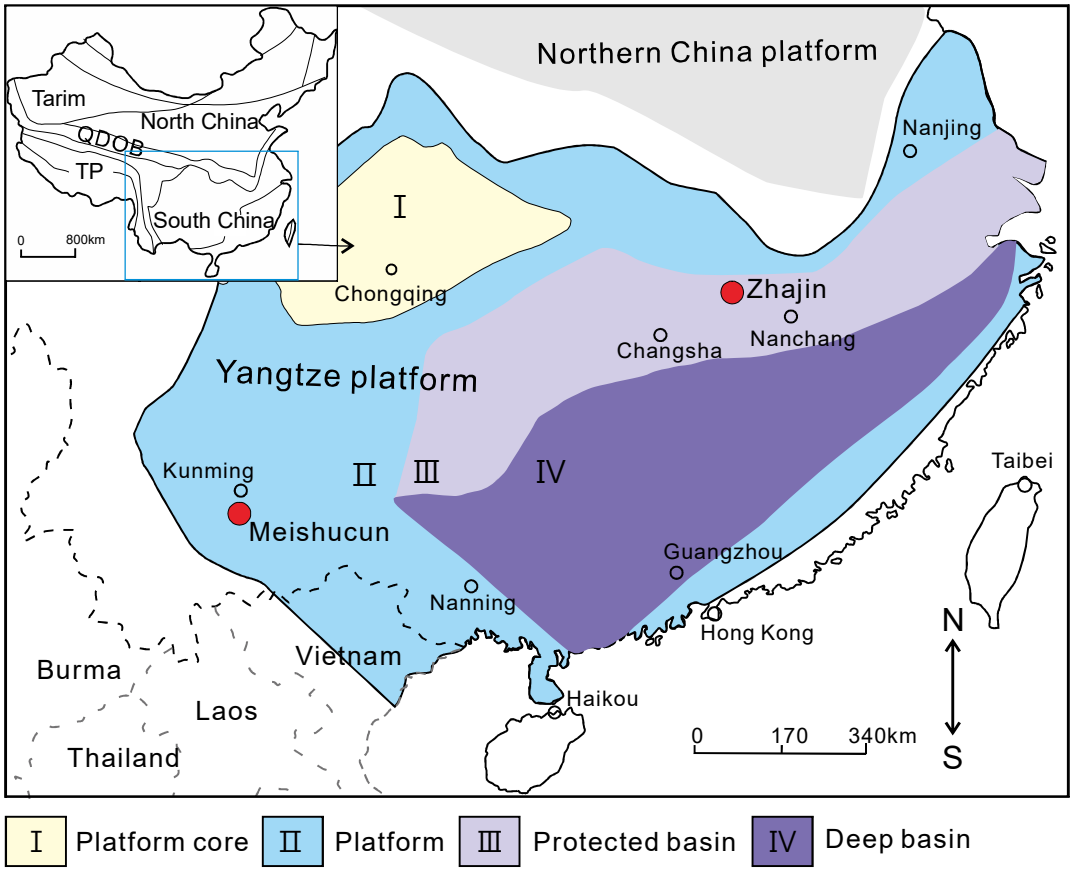

Figure 1

Liu, Z.-R.R., Zhou, M.-F., Williams-Jones, A.E., Wang, W., Gao, J.-F., 2019.
Diagenetic mobilization of Ti and formation of brookite/anatase in early Cambrian black shales, South China.
Chemical Geology, 506: 79-96.

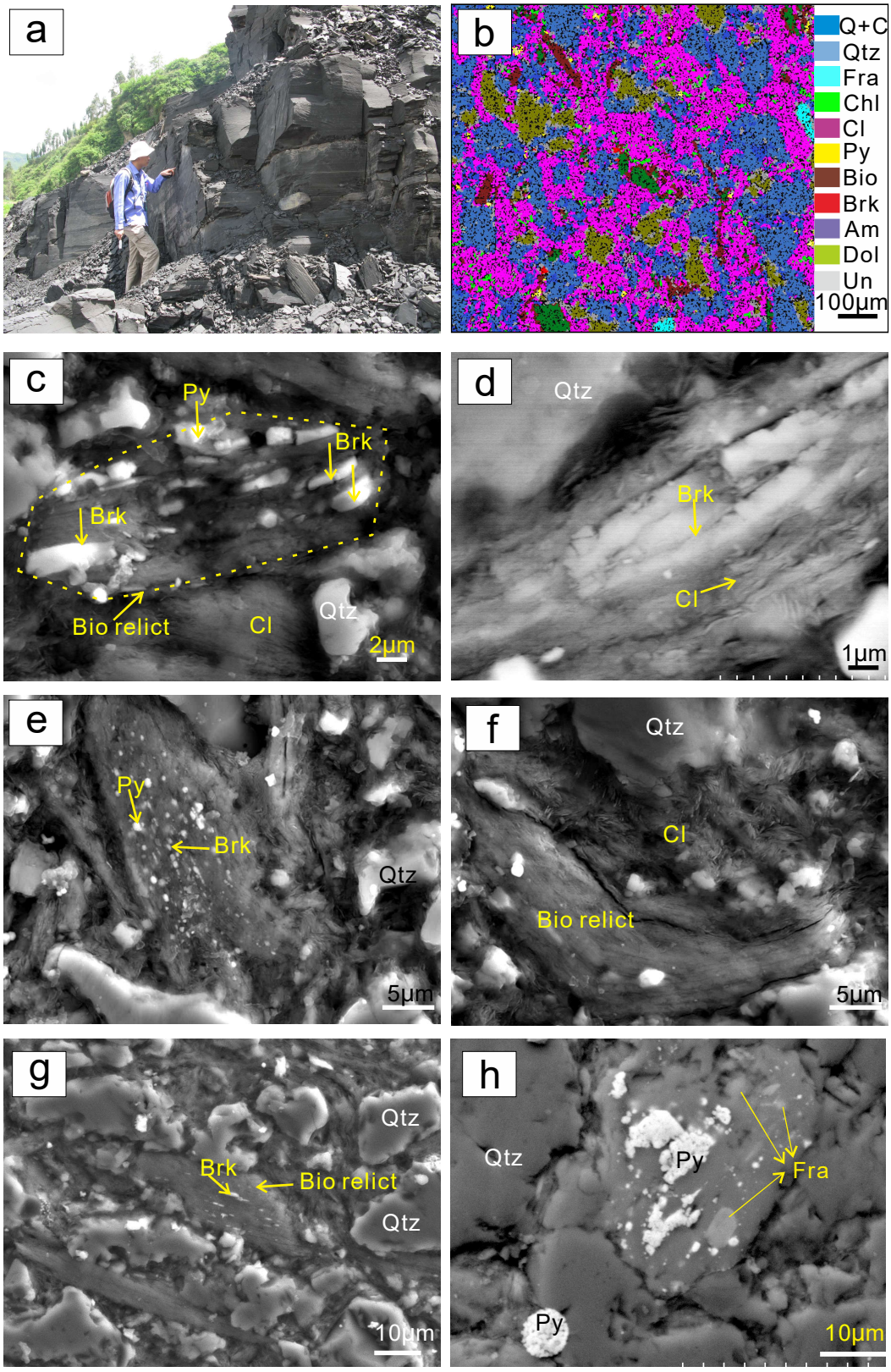

Figure 2

Liu, Z.-R.R., Zhou, M.-F., Williams-Jones, A.E., Wang, W., Gao, J.-F., 2019.
Diagenetic mobilization of Ti and formation of brookite/anatase in early Cambrian black shales, South China.
Chemical Geology, 506: 79-96.

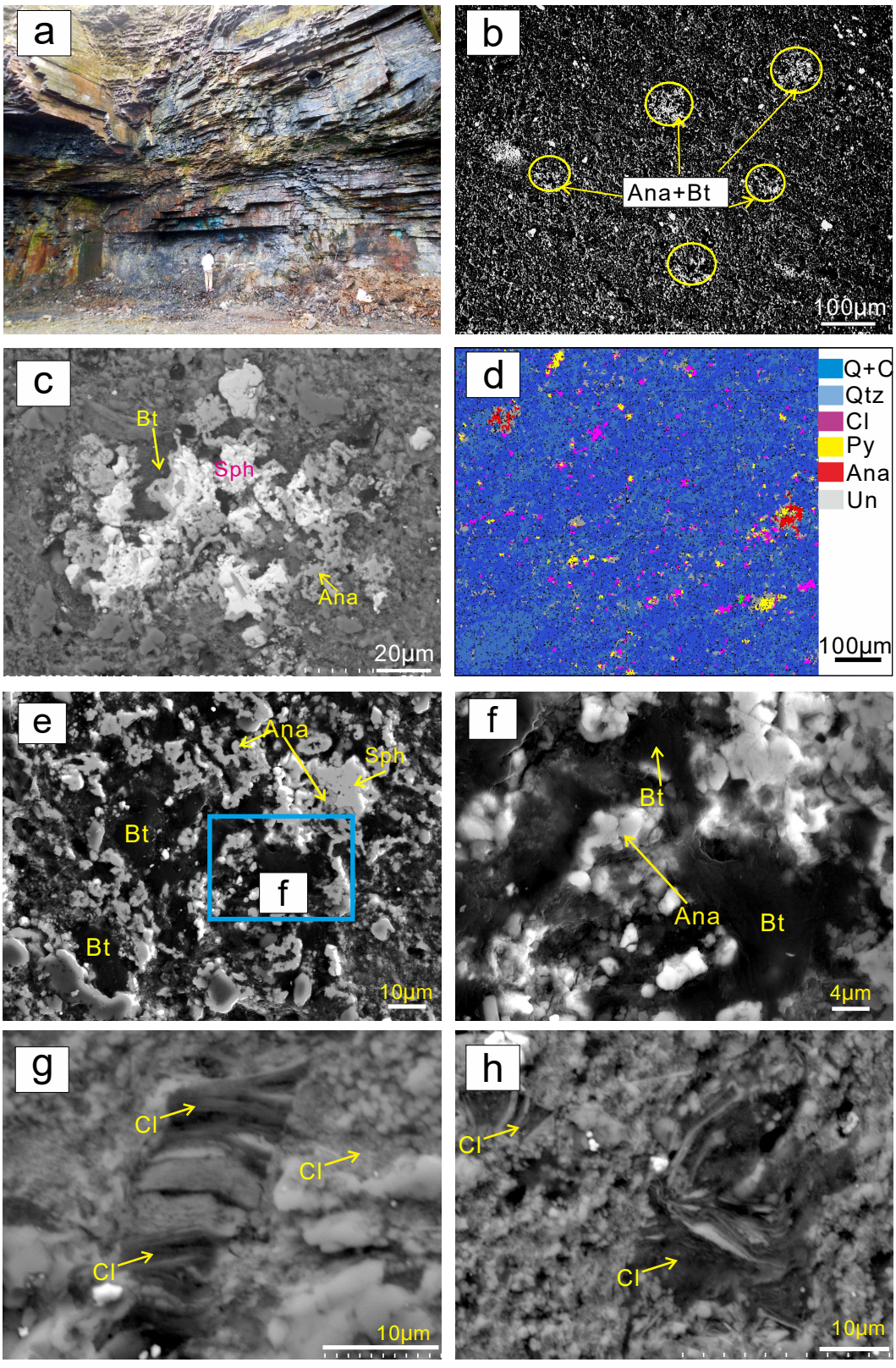

Figure 3

Liu, Z.-R.R., Zhou, M.-F., Williams-Jones, A.E., Wang, W., Gao, J.-F., 2019.
Diagenetic mobilization of Ti and formation of brookite/anatase in early Cambrian black shales, South China.
Chemical Geology, 506: 79-96.

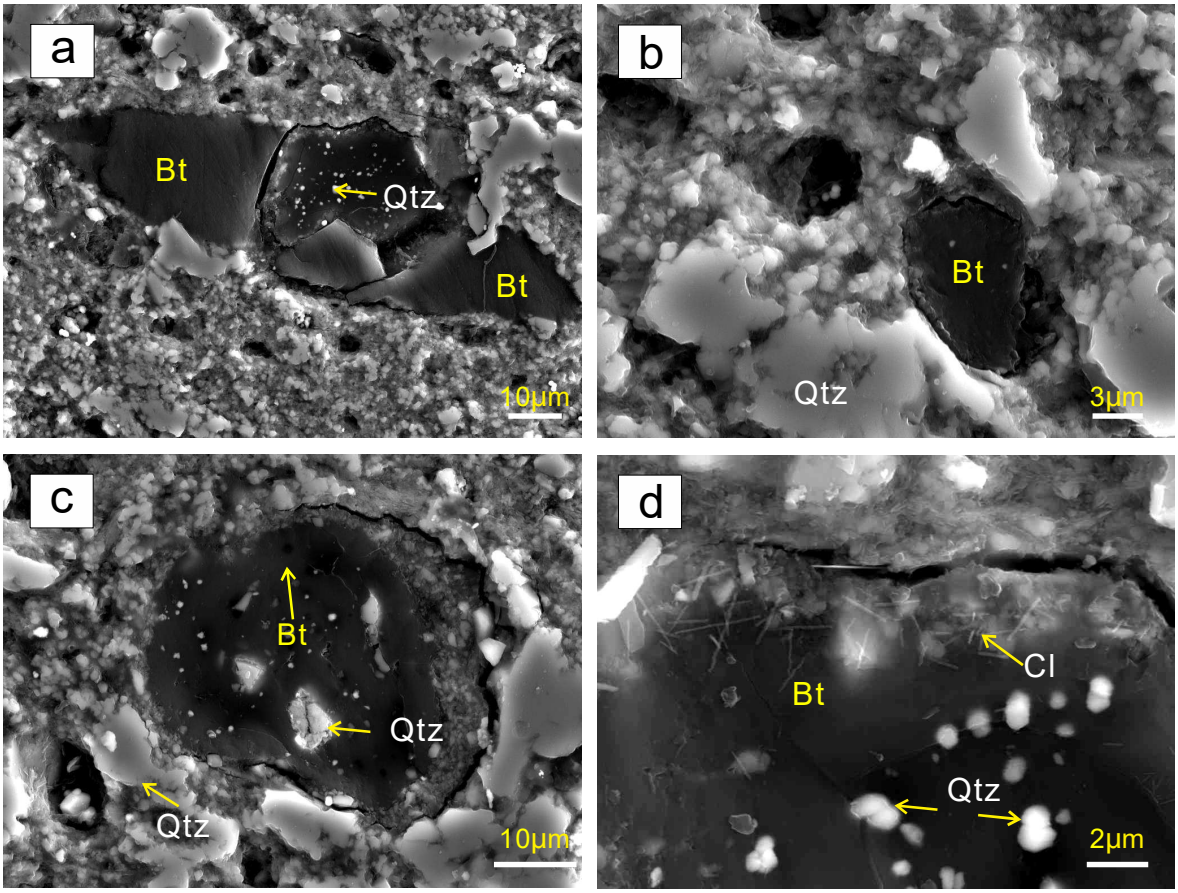

Figure 4

Liu, Z.-R.R., Zhou, M.-F., Williams-Jones, A.E., Wang, W., Gao, J.-F., 2019.
Diagenetic mobilization of Ti and formation of brookite/anatase in early Cambrian black shales, South China.
Chemical Geology, 506: 79-96.

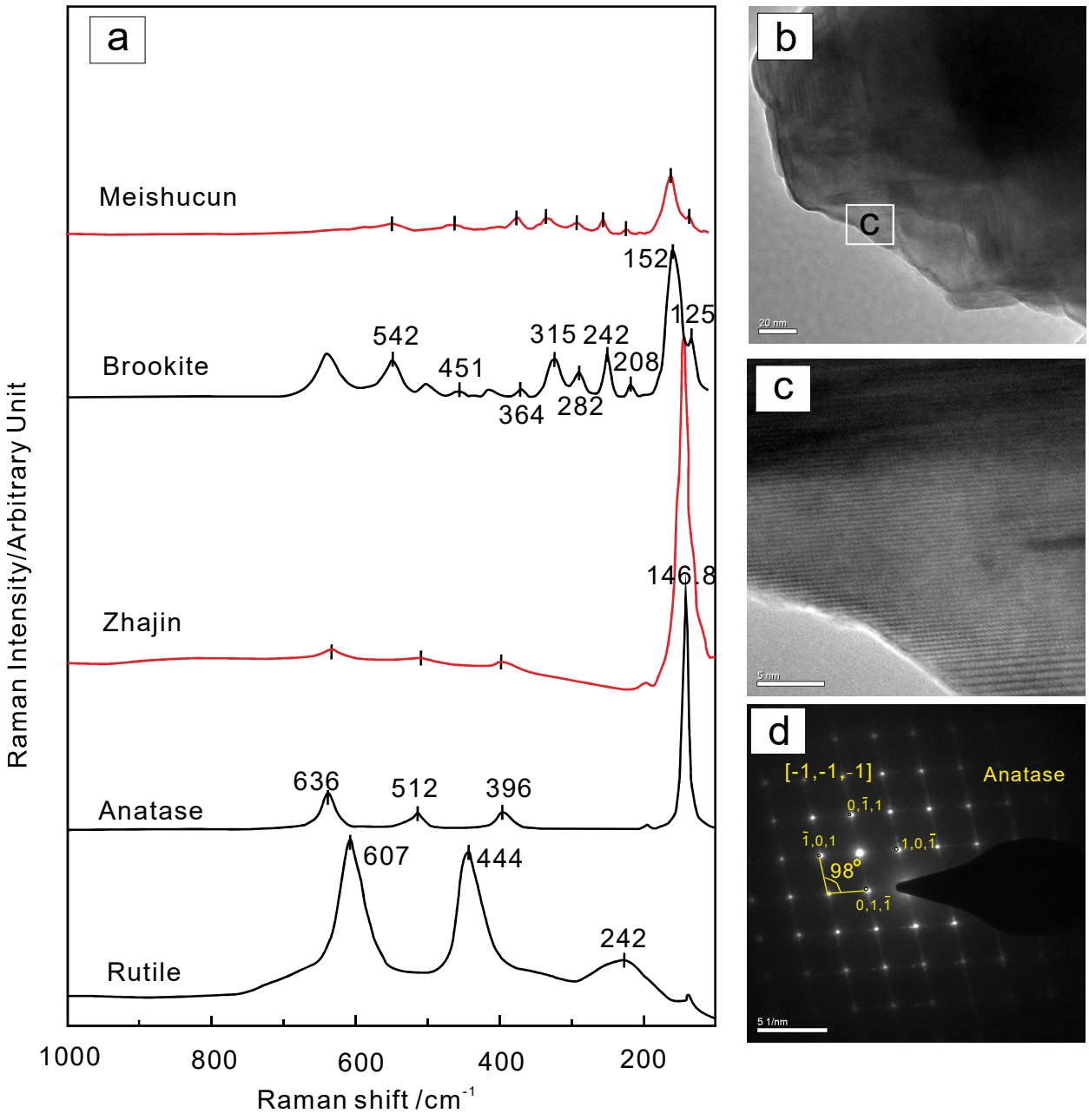

Figure 5

Liu, Z.-R.R., Zhou, M.-F., Williams-Jones, A.E., Wang, W., Gao, J.-F., 2019.
Diagenetic mobilization of Ti and formation of brookite/anatase in early Cambrian black shales, South China.
Chemical Geology, 506: 79-96.

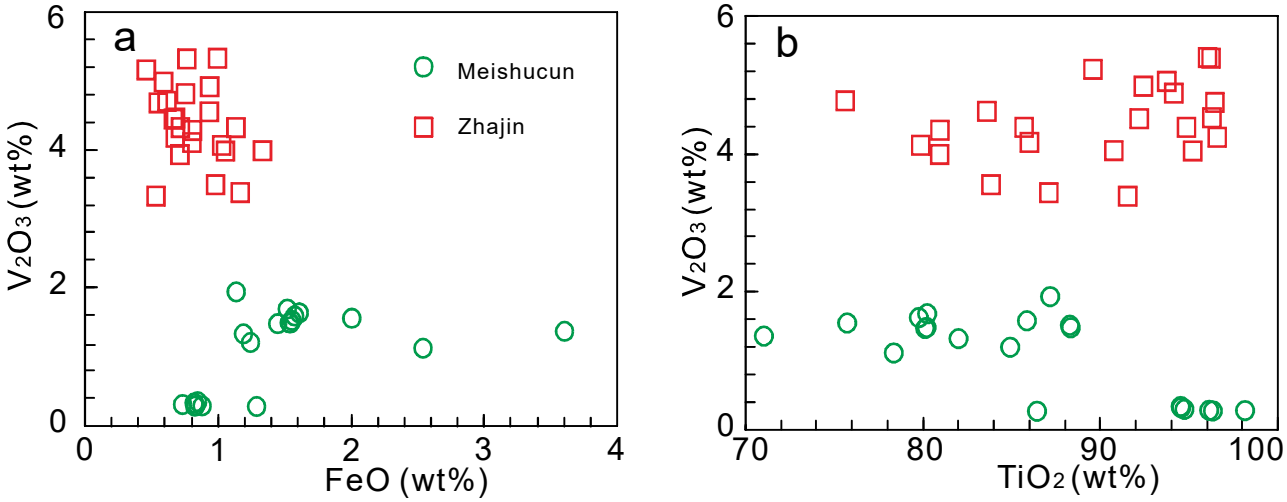

Figure 6

Liu, Z.-R.R., Zhou, M.-F., Williams-Jones, A.E., Wang, W., Gao, J.-F., 2019.
Diagenetic mobilization of Ti and formation of brookite/anatase in early Cambrian black shales, South China.
Chemical Geology, 506: 79-96.

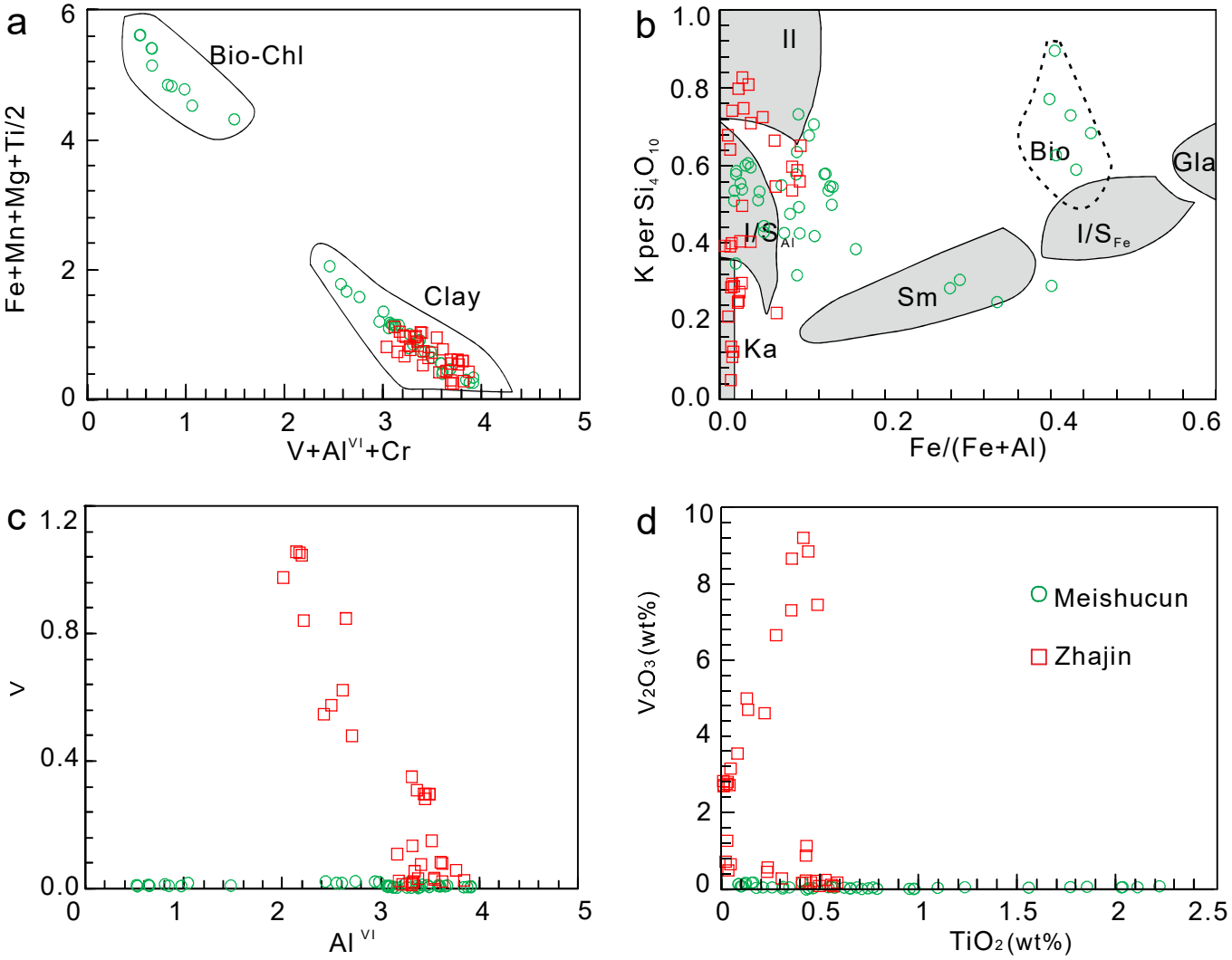

Figure 7

Liu, Z.-R.R., Zhou, M.-F., Williams-Jones, A.E., Wang, W., Gao, J.-F., 2019.
Diagenetic mobilization of Ti and formation of brookite/anatase in early Cambrian black shales, South China.
Chemical Geology, 506: 79-96.

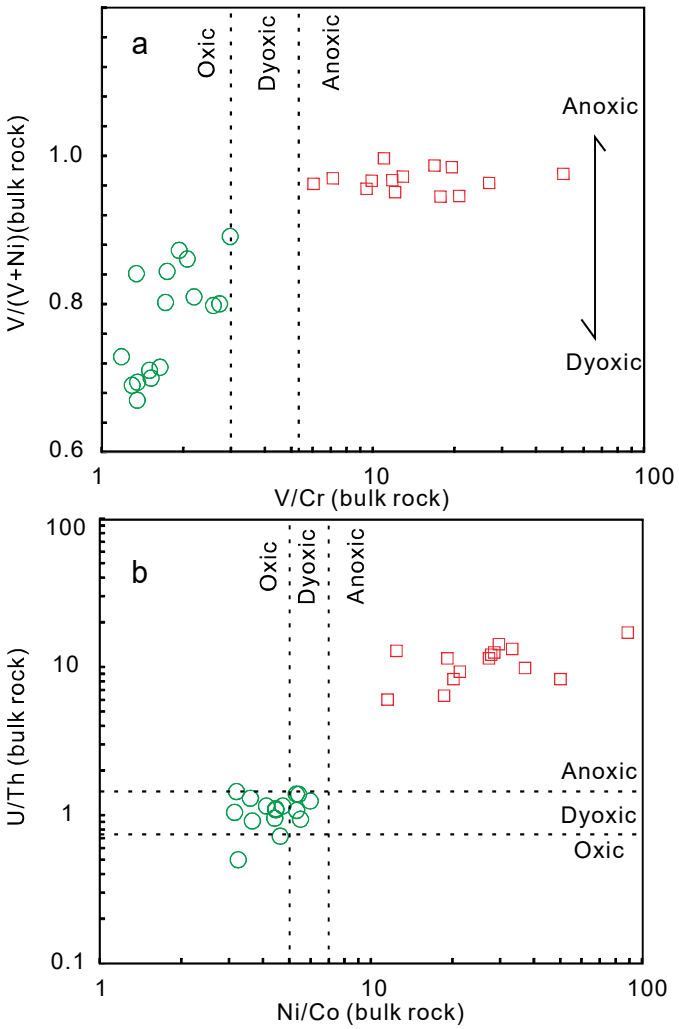

Figure 8